Phase Inversion-Based foam hydrogels for highly efficient Solar-Powered interfacial desalination

Chenyang Xing [a], Zihao Li [a], Shaohui Zhang [c], Jian Bang [a], Zhongjian Xie [b], Han Zhang [a,*], Zhengchun Peng [a,*]

[a] Key Laboratory of Optoelectronic Devices and Systems of Ministry of Education, College of Physics and Optoelectronic Engineering, Shenzhen University, Shenzhen 518060, People's Republic of China
[b] Institute of Pediatrics, Shenzhen Children's Hospital, Shenzhen 518038, People's Republic of China
[c] International Collaborative Laboratory of 2D Materials for Optoelectronics Science and Technology of Ministry of Education, Institute of Microscale Optoelectronics, Shenzhen University, Shenzhen 518060, People's Republic of China

ABSTRACT

Innovative materials are required to promote the development of solar-powered interfacial desalination and purification technologies to address global freshwater scarcities. To this end, evaporators using polymeric hydrogels have been widely studied. However, these systems are slow, energy-intensive, complex, and difficult to operate. New strategies are in urgent need. The present work employs polymeric phase inversion to develop poly (vinyl alcohol) (PVA)-based foam hydrogels, wherein the air bubble phase served as the matrix and cross-linked PVA hydrogel acted as the dispersed phase. In addition, we utilize $Ti_3C_2T_x$ nanosheets-based MXene as the photothermal agent to facilitate the fabrication of hierarchical pore-in-pore structures. The prepared PVA/MXene foam hydrogels exhibit > 95% porosity, as well as high compressibility (>7000 cycles) and very rapid water transport. Importantly, these materials also exhibit remarkably low water evaporation enthalpies. Combined with a new heat supply model, those foam hydrogels achieve an evaporation rate of 4.1 ± 0.1 kg m^{-2}h^{-1} with energy efficiency up to $128.8\% \pm 2.0\%$ under 1 sun irradiation, which is the highest value for MXene-based nanocomposites reported so far. This study demonstrates a significant advancement in solar desalination system by combining phase inversion to make innovative foam materials with optimal external heat management.

1. Introduction

Since the first demonstration of solar-driven interfacial desalination using polymeric hydrogels by Yu et al. in 2018 [1], this technology has been of interest as a means of directly generating potable water [2,3]. This is important because there has been an increasing need for fresh water, partly as a consequence of the global COVID-19 pandemic but also because of population growth, environmental degradation and climate change. In these systems, photothermal agents obtain energy from sunlight and transfer heat to water molecules that subsequently evaporate from hydrogel-air interfaces. Yu's work demonstrated that the internal porous microstructures, surface topography and degree of wetting of the hydrogel determine the interfacial evaporation behavior [4–8]. Water states (bound, intermediate and bulk water) and their relative proportions in the hydrogel can be effectively regulated by designing porous structures, adjusting the polymer backbones to add

hydrophilic functional groups and even by optimizing polymer concentrations. A high proportion of water in the intermediate state reduces the requirement for evaporation energy by significantly decreasing the enthalpy of evaporation (ΔH_E) of the water [9]. Water transport and bumping in a hydrogel can also be affected by the internal porous architecture based on capillary effects and the balance between these phenomena and the evaporation of surface water. A continuous and timely bottom water supply has been shown to suppress the crystallization of salt at the hydrogel surface in response to exposure to intense sunlight. Energy nanoconfinement has also been reported to be correlated with the degree of porosity [3]. In addition, the evaporation of water is related to various hydrogel surface properties, including surface structures [10] and wetting behavior [11]. The former directly determines the optical path length and thus the net absorption of solar radiation while the latter is typically related to the heat flux of the evaporated water steam. In spite of much effort having been devoted to

precisely adjusting the physical properties of hydrogels so as to meet the requirements noted above, further improvements are required. Specifically, the use of these systems is often time-consuming and involves complex processes and designs. As representative examples, the well-known hierarchical PVA/PPy [1] and PVA/rGO-based hydrogels [2] must be prepared using repeated freeze–thaw cycles, meaning that these materials may not be reproducible. Another recent strategy involves the preparation of PVA hydrogels via a self-assembled templating strategy [12]. This technique provides materials with interconnected pores and good elasticity that exhibit high evaporation rates in response to sunlight. The most important aspect of this prior work was the use of sacrificial poly(methyl methacrylate) (PMMA) microsphere templates to provide tunable water channels. Unfortunately, this process necessitates etching of the PMMA with acetone and the complete removal of the PMMA template requires careful attention. Therefore, it would be desirable to design and develop simpler but more general approaches to the synthesis of porous hydrogels exhibiting high evaporation efficiencies and suitable mechanical properties.

Surfactant-based foaming strategies have been used to generate pores within three-dimensional (3D) graphene hydrogels, using compounds such as alkyl polyglucosides [13] and sodium dodecyl sulfate (SDS) [14]. With the help of these surfactants, rapid stirring of precursor graphene oxide (GO) dispersion will generate a considerable number of microbubbles that can produce highly porous 3D graphenes. In this process, GO nanosheets having two-dimensional (2D) morphologies are affixed onto the surfaces of the bubbles such that they are stabilized. Recently, Zong's group reported the first-ever SDS-foamed PVA/Janus-like GO hybrid hydrogels [15]. These materials were made using SDS in conjunction with stirring at 2000 rpm to produce hydrogels with hierarchical porous morphologies. This prior work suggests the viability of a foam-based phase inversion concept. In Zong's study [15], bubbles were dispersed at a low volume fraction, ϕ_b, within a hydrogel phase (accounting for a large volume fraction, ϕ_h, based on the total volume of the polymer and water) when using a moderate stirring rate. In the case that a higher stirring rate was applied, ϕ_b was increased accordingly as a result of the excellent foaming ability of the viscous PVA solutions. In trials for which $\phi_b \gg \phi_h$, the bubble phase acted as the matrix while the hydrogel was the dispersed phase, resulting in complete phase conversion. Consequently, additional cross-linking gave a new type of foam hydrogel having a highly porous interior structure with rough surfaces. Importantly, the extremely high porosity of these materials made them compressible and allowed rapid water transport. These properties are very promising with regard to solar evaporation applications, although such uses have not yet been realized.

The materials known as MXenes, comprising 2D metal carbides and nitrides, were first reported in 2011 [16] and have since been applied in the fields of energy, environmental remediation, biomedicine and electronics [17–19]. MXenes not only exhibit exceptional electrical conductivity but can also serve as photothermal agents providing almost 100% light-to-heat conversion efficiency [20], primarily because of the high electron density of states near the Fermi level of each such material [21]. MXenes can have a wide range of compositions, are hydrophilic and show mass productability. Based on these inherent advantages, MXene-based nanocomposites have been applied in evaporation systems in the form of 3D inorganic porous macroscopic monolithic aerogels [22–29], vacuum-assisted filtration induced membranes [30–34], composite hydrogels [35–38], and coated 3D skeletons [39–45], membranes [46–50] or fabrics [51–54]. However, in the case of inorganic materials such as these, poor mechanical strength is often observed, along with inferior evaporation performance. Therefore, the design of MXene-based evaporators should be improved to allow for applications in solar desalination systems.

The present work built on the foam phase inversion concept noted above by employing super-high-speed stirring (35,000 rpm) to agitate and foam PVA/MXene solutions. In addition, a triblock copolymer (F-127) was used to further stabilize the resulting microbubbles via a cross-linking reaction to produce strong materials. Interestingly, the highly dispersed PVA hydrogel phase formed through this process was found to be stable and to accommodate the bubble phase to produce foam hydrogels with typical pore-in-pore surface microstructures and high porosities (in excess of 95%). As a result of the unique construction of these foam hydrogels, they provided rapid water transport, a high degree of water uptake, a reduced ΔH_E value and excellent compressibility. The present study also presents the first heat supply model for high performance evaporation applications that differs significantly from the standard heat isolation model. The present PVA/F-127/MXene foam hydrogels demonstrated an evaporation rate of 4.1 ± 0.1 kg m^{-2}h^{-1} with an energy efficiency as high as $128.8\% \pm 2.0\%$ under 1 sun irradiation. This represents the highest performance to date for a MXene-based nanocomposite and also outperforms other similar systems.

2. Experimental and calculation

2.1. Fabrication strategies

2.1.1. Fabrication of 2D MXene

A 2D MXene colloidal solution was prepared according to a procedure employed in our previous study [55]. Prior to use, its concentration was determined to approximate 11 mg/mL using vacuum-assisted filtration method and it was stored at 4 °C after being purged with argon to remove residual dissolved oxygen.

2.1.2. Fabrication of a PVA-based hydrogel and foam hydrogels

A typical PVA hydrogel was prepared using a cross-linking strategy. Briefly, 4 g of a 10 wt% PVA aqueous solution (using PVA with a Mw of approximately 67,000) was thoroughly mixed with 0.2 mL of a 50 wt% glutaraldehyde (GA) solution, 1.2 mL water and 0.2 mL of a 1.2 M HCl solution. The resulting cross-linking reaction proceeded too rapidly at room temperature and so the mixing process was conducted at 0 °C to ensure a completely homogeneous state. After mixing, the solution was sonicated to remove bubbles caused by agitation. The final PVA hydrogel was obtained by heating the mixture at 40 °C for 10 min followed by dialysis with water for several days.

The PVA foam hydrogels were prepared using a combined bubble-foaming and cross-linking strategy. Briefly, a homogeneous PVA/GA/H$_2$O/HCl mixture (having the same composition as in the PVA hydrogel described above) was cooled to 0 °C and then stirred using a high-speed mechanical agitation device at 35,000 rpm for 180 s. Numerous microbubbles were generated during the first 120 s and got a boost and subsequent stable state in numbers during the last 60 s. The mixture was subsequently transferred into a container and quickly immersed in a 40 °C oil bath for 10 min to produce the PVA foam hydrogel. This was followed by immersion of the gel in hot water with repeated manual squeezing such that the bubbles within the specimen were replaced with water to give the finished product. Subsequent dialysis in water assisted in removing residual impurities, including traces of acid.

The PVA/F-127 foam hydrogel was prepared using the same process except that 0.2 mL of a 100 mg/mL Pluronic F-127 solution (using F-127 having a molar mass of approximately 12,600 g/mol, EO$_{106}$PO$_{70}$EO$_{106}$) was added while removing the equivalent volume of water from the PVA/GA/H$_2$O/HCl mixture. That is, the sample was made using 1 mL water together with 0.2 mL F-127. This sample is referred to herein as P-F-0.2. In some specimens, the concentration of F-127 was varied while maintaining a constant system volume by changing the amount of water in the formulation. These samples are referred to herein as P-F-X, where X denotes the volume of F-127 solution used.

2.1.3. Fabrication of PVA/MXene/F-127 foam hydrogels

Various PVA/MXene/F-127 foam hydrogels were produced by first thoroughly mixing a MXene solution with a PVA solution followed by the addition of an F-127 solution, HCl and water. Note that the final mixtures had the same volume as that of the PVA hydrogel and PVA

foam hydrogel specimens (with or without F-127). Each precursor solution was subsequently stirred at 35,000 rpm while being held at 0 °C for 180 s, followed by promotion of the cross-linking reaction, manual squeezing and dialysis to generate the final PVA/MXene/F-127 foam hydrogel. These materials are referred to herein as P-F–M–X, where X denotes the volume of MXene solution used. Details concerning the formulations of the PVA-based hydrogels and foam hydrogels are provided in Table S1 of the supporting information.

2.2. Characterization

2.2.1. Morphological and physical property characterization

The surface and cross-sectional morphologies of the various freeze-dried gel samples were observed using scanning electron microscopy (SEM). The crystallinity of the PVA in each material was also evaluated using X-ray diffraction (XRD) with a scanning speed of 1°/min. The physical interactions of the various components in these materials were ascertained using Raman microscopy with an excitation wavelength of 633 nm at room temperature. The porosities of the samples were evaluated via the mercury intrusion method, using six samples from each batch and reporting average values. Spectra of dried and seawater-wetted foam hydrogels were acquired using a UV–visible-near infrared (NIR) absorbance spectrometer over the range of 200–2500 nm, evaluating both reflection and transmittance contributions. The mechanical properties of the materials under compression were evaluated using an Instron instrument with frequencies of 0.5 and 0.8 Hz, respectively. The thermal stability of each specimen was monitored by thermogravimetric analysis (TGA) with heating from ambient temperature to 700 °C at a heating rate of 20 °C/min under argon.

2.2.2. Evaporation enthalpy (ΔH_E)

The enthalpy of evaporation of the water in hydrogel- or foam-hydrogel-based samples was calculated using the Eq. (1) [12].

$$U_{in} = E_{equ}m_g = E_0m_0 \tag{1}$$

where E_0 and m_0 are the enthalpy of evaporation (2450 J/g, theoretical value of liquid water) and the change in the mass of water under dark conditions (that is, the values obtained during the control group experiments), m_g is the change in the mass of the samples under the same conditions, and E_{equ} is the enthalpy of evaporation of water in the sample as calculated using Eq. (1). The calculated equivalent enthalpy of evaporation values was subsequently used to determine the energy efficiency.

In brief, each specimen was saturated with water, weighed, and then transferred into a sealed drying vessel together with a saturated potassium carbonate solution (enabling stabilized RH of ca. 45%). A quantity of pure water was also transferred into a beaker, such that the exposed surface area of this water was equal to that of the samples, and then weighed. This beaker was subsequently placed in a sealed drying container together with a saturated potassium carbonate solution. After 30 min, the sample was removed and weighed to obtain m_g, the change in mass. Similarly, the pure water was removed and weighed to obtain the mass change. The enthalpy of evaporation, E_{equ}, of the sample was calculated using the equation given above. These calculations used the averages of more than five replicate measurements performed with different samples from different batches.

2.2.3. Seawater evaporation behavior

Actual seawater from Shenzhen Bay, China, was filtered to remove various solids and then used as a test sample. The foam hydrogels (which floated on water) were directly placed onto these seawater samples in containers surrounded by either a white foam that provided insulation from heat or a black foam that absorbed heat. These scenarios represented contrasting heat isolation and heat supply models. Each specimen was exposed to simulated sunlight at 1 sun and changes in mass and

temperature were monitored using an electronic balance and infrared thermal imager. The evaporation rate was determined by calculating the mass decrease during each 60 min evaporation trial with a specific amount of evaporation surface exposed after subtracting the evaporation observed under dark conditions.

Energy efficiency. The seawater desalination performance of each MXene foam hydrogel specimen was evaluated using the standard solar radiation intensity. The corresponding solar-to-vapor efficiency (η) was calculated as

$$\eta = \left(\dot{m}E_{equ} \right) / C_{opt} \, P_0 \tag{2}$$

where $\dot{m}$ is the mass flux, given by the laboratory steady state, P_0 is the solar irradiation power (1 kW m^{-2}), C_{opt} is the optical concentration, and E_{equ} is the equivalent enthalpy of evaporation of water in the MXene foam hydrogel determined by comparing the evaporation of the sample with that of bulk water under dark conditions.

Experimental trials monitoring evaporation in response to exterior natural daylight were conducted between 8:00 a.m. and 6:00 p.m. from September 1st to October 10th, 2022, at the Canghai campus of Shenzhen University in Nanshan District, Shenzhen, China. The quality of the water collected from various trials was ascertained by quantifying the concentrations of four main inorganic ions (Na^+, K^+, Ca^{2+} and Mg^{2+}) using inductively coupled plasma–atomic emission spectroscopy. The evaporation performance under natural sunlight was evaluated by monitoring variations in the mass of the seawater sample, the sunlight intensity and the outdoor temperature at various intervals over a span of 32 days.

2.3. COMSOL simulation method

2.3.1. Water transport

Numerical simulations of water transport in the MXene-based foam hydrogels were conducted using the COMSOL Multiphysics 5.4 software package. The specimen geometry employed during these simulations was constructed to have the same dimensions and a similar shape to those of the samples. The mass transfer process in the model included two-phase flow, liquid phase transport and vapor phase transport. In the case of the two-phase flow, the sample could be considered as a porous solid matrix with the saturation moist air (S_g) and water (S_l) flows in the porous gel having the constraint

$$S_g + S_l = 1 \tag{3}$$

The flow field, μ_g, and pressure distribution, p_g, of moist air in the porous medium were calculated using the Brinkman equation, written as

$$0 = -\nabla p_g + \nabla \frac{\mu}{\varepsilon} \left(\nabla \mu_g + \nabla \mu_g^T \right) - \frac{\mu}{\kappa} u_g \tag{4}$$

where p_g is the pressure of moisture air, μ_g is Darcy's velocity field, μ is the dynamic viscosity of the fluid, ε is the porosity of the medium, and κ is the permeability of the medium. The liquid water transport velocity in the porous sample was simulated using a combination of Darcy's Law and COMSOL simulation of water transport. These calculations employed the equation

$$u_l = -\frac{\kappa_l}{\mu_l} \nabla p_l \tag{5}$$

where k_l, μ_l and ∇p_l are the permeability, viscosity and pressure gradient of the liquid phase within the MXene-based sample, respectively. The mass transport of the liquid phase inside the porous domain could be determined using the relationship

$$\frac{\partial c}{\partial t} + \nabla \bullet J = R \tag{6}$$

where J is the diffusion flux of water and R is the water mass lost by evaporation. The water vapor transfer velocity was defined as

$$\mu = \frac{\mu_g}{Sg\varepsilon} - M_a \frac{\rho_g}{Mg^2} D_{eff} \nabla \left(\frac{M_g}{\rho_g} \right) \tag{7}$$

where M_g and ρ_g are the mass and density of the moist air, respectively, M_a is the mass of air, and D_{eff} is the effective diffusivity for two components. The latter variable is defined by the Millington-Quirk equation as

$$D_{eff} = D_{va} \varepsilon^{4/3} S_g^{10/} \tag{8}$$

where D_{va} is the vapor-air diffusivity and has a value of 2.6×10^{-5} m² s⁻¹. Considering the confinement of water in the polymeric network and convection through air, the heat transfer near the surface could be described by the equation

$$E = \rho C_{p,tot} \frac{\partial T}{\partial t} + \rho C_{p,tot} \mu \bullet \nabla T + \nabla [k \nabla T] \tag{9}$$

where E is the thermal energy input from optical-thermal conversion and ρ, $C_{p,tot}$ and k_{tot} are the total density, heat capacity and thermal conductivity of the moist air and liquid phase, respectively. The latent heat source within the MXene-based foam hydrogel network, Q_{evap}, was calculated as

$$Q_{evap} = -H_{evap} \bullet m_{evap} \tag{10}$$

where H_{evap} is the latent heat of evaporation and m_{evap} is the evaporation flux at the sample top surface.

Temperature distribution. Considering the confinement of water in the polymeric network and the extent of convection in the internal gaps and micron-sized channels, the heat transfer in the sample was

$$E_{in} = \rho C_p \frac{\partial T(x,t)}{\partial t} + \rho C_p v \bullet \nabla T(x,t) + \nabla [k \nabla T(x,t)] \tag{11}$$

where x and t are the space vector and time, respectively, ρ, C_p and T (x, t) are the mass density, liquid thermal capacity and local temperature, respectively, and ν and k are the fluid flow rate and thermal conductivity of the aqueous medium. Here, E_{in} represents the thermal energy input from optical-thermal conversion. Based on a previous report, the heat transfer model was simplified by using a semi-infinite medium. The numerical simulations were conducted using the COMSOL Multiphysics 5.4 package in the steady and transient analysis modes. A constant heat flux of 0.1 kW m⁻² was applied to the top of the sample (Z = 500), corresponding to the solar energy input at the surface of the actual hydrogel, which resulted in evaporation that consumed energy on the order of 0.9 kW m⁻². The resulting two-dimensional model was discretized into 1000 elements and convective heat transfer in the polymeric network was disabled to simulate the water restriction effect. Qualitative analyses were performed by setting the ambient and water temperatures to 20 °C and employing an equilibrium heat flux of 0.1 kW m⁻². During the transient mode simulation, the initial and final conditions were set to t = 1 s and t = 6000 s, respectively. As a consequence, the temperature distribution in the MXene-based samples varied slightly over time because of the continuous photothermal conversion (resulting in heating) and evaporation (resulting in cooling) occurring in the vicinity of the surface.

3. Results and discussion

3.1. Use of the foam phase inversion concept to fabricate foam hydrogels

PVA solutions are known to readily generate bubbles in response to mechanical agitation. In some cases, a relatively low quantity of small bubbles is obtained and so the bubbles can be considered as the dispersed phase while the PVA solution is the matrix phase. However, in the case that the relative quantities of the two phases are reversed (that is, the bubbles form the matrix while the PVA solution is the dispersed

phase), an intriguing new lightweight, compressible functional material having hierarchical pores can be obtained. The PVA chains typically act as a surfactant to temporarily stabilize the bubbles induced by agitation, and so incorporating an additional surfactant would be expected to provide greater numbers of more uniform bubbles and improved stability. The addition of a cross-linking agent to chemically bond the PVA chains to one another could also cause the bubbles to be retained, thus producing a robust, compressible foam hydrogel.

The foam phase inversion concept used to synthesize foam hydrogels in the present work is illustrated in Fig. 1. In **Stage I** of this process, the PVA (acting as the matrix), MXene nanosheets (the photothermal agent) (**Supporting Information of Fig. S1**), F-127 (the bubble stabilizer), GA (the cross-linking agent), HCl (the acid catalyst) and water (the solvent) were mixed at 500 rpm to produce a homogeneous solution containing a limited amount of small bubbles. More rapid mixing induced foaming that was followed by a thermally accelerated cross-linking reaction as **Stage II**. This mixing produced a considerable number of bubbles accompanied by an obvious increase in the system volume. This system can be imagined as equivalent to spheres of varying volumes filled with air that are connected with one another by the cross-linked PVA chains. These spheres account for the majority of the overall volume of the material. In addition, because the water and MXene components of the hydrogel cannot fill the air bubbles, these components can only be located at surfaces or interfaces between bubbles. As a result, the gaps between bubbles comprise PVA chains, MXene nanosheets and water. After cross-linking, the PVA/F-127/MXene/GA/HCl/H₂O system is made of bubbles with hydrogel between the bubbles, meaning that this system is a foam hydrogel. In **Stage III**, the air in the bubbles is replaced with water so that the foam hydrogels are actually made of water-filled pores connected via cross-linked PVA/MXene chains.

A portable homogenizer (**Supporting Information of Fig. S2**) was used to carry out the high-speed agitation of PVA/MXene solutions with various MXene concentrations. Upon stirring at 35,000 rpm, numerous bubbles were formed in the PVA or PVA/MXene solutions and these systems became white (Fig. 2a) or dark green (Fig. 2b). It should also be noted that these bubbles increased the viscosity of the solution so that it no longer flowed (**Supporting Information of Video S1-S3**), indicating a high degree of foaming. Consequently, each material could only be transferred to other vessels by manual scraping of the foam from the container walls. These bubbles before the cross-linking were directly visualized by using polarized optical microscopy. In the case of the PVA system without F-127 (**Supporting Information of Fig. S3**), some very large bubbles were obtained (approximately 600 μm in diameter) and there was a wide range of bubble sizes. After adding the F-127 (Fig. 2c), this size range was decreased, indicating that the F-127 further stabilized the bubbles and hindered coalescence. Introducing the MXene nanosheets (Fig. 2d) had little effect on the generation and coalescence of bubbles although the size range was reduced relative to that of the PVA/F-127 system. In addition, the bubbles in the PVA/F-127/MXene system were obviously thicker (Fig. 2d). In fact, the bubble thickness increased with increases in the MXene concentration, along with a slight decrease in the bubble size (**Supporting Information of Fig. S3 and Fig. S4**). That is, the introduction of MXene further increased surface viscosity and thickness of the foam film and thus effectively decreased the influence of film drainage phenomenon. Fig. 2e compares the four types of PVA-based samples, including the PVA hydrogel (processed at 500 rpm), PVA foam hydrogel, PVA/F-127 foam hydrogel (P-F-0.2) and PVA/F-127/MXene foam hydrogel (P-F-M−1). The bubble-filled PVA and PVA/MXene solutions generated by rapid mixing had significantly increased volumes (**Supporting Information of Fig. S5**). After cross-linking, the PVA-based foam hydrogels were also found to float on water, confirming their porous nature (Fig. 2e). Interestingly, a standard PVA hydrogel did not float, even though this material was porous (Fig. 2e). These results suggest that the present foam hydrogels had multiple porosity structures and were less dense than hydrogels. The PVA-based foam hydrogels were soft, highly compressible and relatively
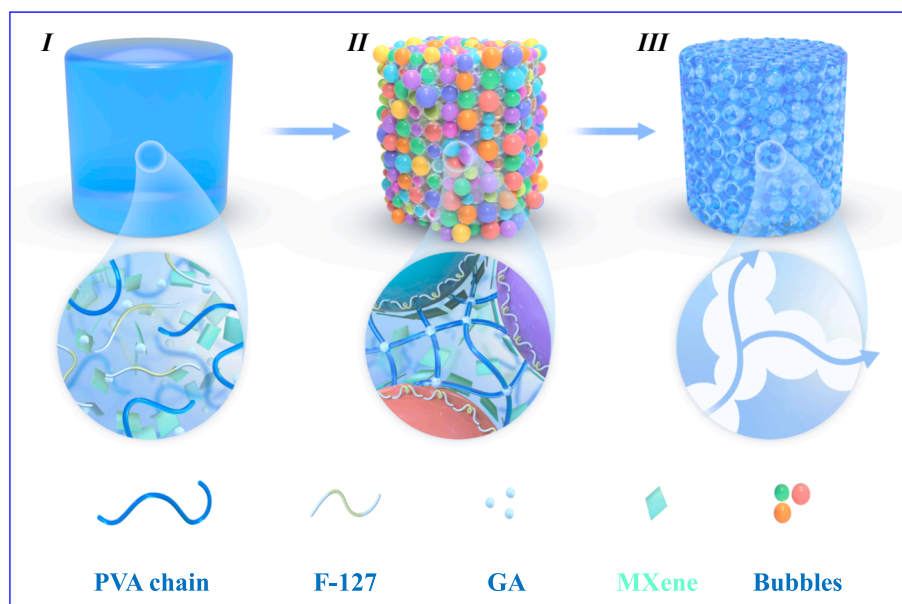
Fig. 1. The foam phase inversion strategy used to create robust and compressible PVA/F-127/MXene foam hydrogels. Diagrams illustrating the three preparation stages. **Stage I**: a homogeneous precursor solution is prepared, including PVA chains (the matrix), F-127 (the surfactant), MXene nanosheets (the nano-photothermal agent), GA (the cross-linking agent), HCl (the acid catalyst) and water (the solvent). **Stage II**: a cross-linked gel containing numerous microbubbles having various diameters is generated. **Stage III**: a foam hydrogel state with a hierarchical multi-porous structure and multichannel pathways for water migration is produced.

strong while the PVA hydrogel was somewhat rigid (Fig. 2**f**). In addition, the as-prepared PVA/F-127/MXene foam aerogel was sufficiently lightweight that a sample could be held up on a Setaria Viridis plant (Fig. 2**g**). This material also exhibited rough top and bottom surfaces (Fig. 2**g**), in contrast to the glossy surfaces of the PVA hydrogel (Fig. 2**f**). Large-scale production of this foam hydrogel was also exploited, as presented in Fig. 2**h and 2i**, respectively, again confirming their favorite self-floating feature (**Supporting Information of Fig. S6**). The PVA/F-127/MXene foam hydrogels having various MXene contents all exhibited exceptional compressibility (**Supporting Information of Fig. S7**), indicating that the addition of the MXene had little effect on this property. In addition, the PVA/F-127/MXene (P-F-M−1) with the highest MXene content was found to be able to withstand at least 7000 compressions without any evidence of damage (Fig. 2**j** and **Supporting Information of Fig. S8**).

3.2. Microstructure characterization

The surface structures of solar absorbers have a significant effect on their absorbance and transmittance properties as well as their refraction characteristics. SEM images of the surface and cross-sectional microstructures of PVA, PVA/F-127 (P-F-0.2) and PVA/F-127/MXene (P-F-M−1) specimens are displayed in Fig. 3. The PVA hydrogel does not show a porous surface structure but rather has a compact morphology (Fig. 3**a**). In contrast, many distinct pores of various sizes and shapes can be readily observed in the foam hydrogels (Fig. 3**b, c and d**). The PVA foam hydrogel without the F-127 contained many irregular circular pores having smooth walls (Fig. 3**b**). Following F-127 addition, rough networks appeared in the matrix and even on the pore walls (Fig. 3**c**). Interestingly, in the case of the PVA/F-127/MXene foam hydrogel (Fig. 3**d**), many small structures can be observed along with a typical hierarchical pore-in-pore structure. In such cases, a single large pore will contain many small pores along with even smaller pores on the pore walls (Fig. 3**e**). Images of these specimens at increased magnifications also indicate their cellular structures (Fig. 3**g and 3 h**). The flat matrices of these materials were evidently interspersed with large pores to form 3D polymeric networks (Fig. 3**i-l**), suggesting the presence of very rough surface structures. These surface microstructures would be expected to determine the solar absorption characteristics, horizontal water transport properties and even the heat fluxes exhibited by the gels. The cross-sectional structure of the PVA/F-127/MXene foam hydrogel is shown in Fig. 3**m-p**, which demonstrate the highly porous morphology of this

material. This structure is necessary for vertical water transport. Elemental mapping images indicating the distributions of C, O, F and Ti are presented in Fig. 3**q-t** and confirm the homogeneous dispersion of the MXene in the PVA matrix.

3.3. Physical properties

The crystallinity of each specimen was evaluated using XRD. The patterns in Fig. 4**a** show that the original PVA pellets generated two sharp peaks at 19.5° and 40.3° that are typical of the (1 0 1) and (1 1 1) planes of semi-crystalline PVA, respectively. An additional weak shoulder peak at 22.9° resulting from the (1 0 1) crystal plane can also be observed. However, after foaming, the crystallinity of the PVA was reduced. As an example, the intensity of the (1 0 1) peak obtained from the PVA foam hydrogel was considerably decreased with an accompanying increase in the full width at half-maximum (FWHM) value. This lower degree of crystallization is also reflected in the disappearance of the peaks related to the (1 0 1) and (1 1 1) planes. Similar trends were also found in the patterns obtained from the PVA/F-127 and PVA/F-127/MXene foam hydrogels. These results imply that the introduction of bubbles may restrict the intermolecular interactions of the PVA chains and consequently impair their crystallization. The reduced crystallization of the foam hydrogels was confirmed by the Raman spectra acquired from these specimens (**Supporting Information of Fig. S9**). Fig. 4**b** plots the water transport properties of the PVA/F-127/MXene foam hydrogels. After only 10 s, the PVA/F-127/MXene (P-F-M−0.125) was able to absorb a quantity of water equal to 1750% of its mass, with a water uptake rate as high as 175%/s. This uptake was observed to plateau approximately another 10 s later. Increases in the MXene content of the PVA/F-127/MXene foam hydrogel increased the absolute water uptake as well as the uptake rate. This result is considered reasonable because these foam hydrogels had pore-in-pore microstructures and the MXene nanofiller was hydrophilic and so induced a strong capillary force that promoted rapid water transport, especially in the vertical direction. These foam hydrogels also exhibited outstanding water retention and enhanced thermal stability (**Supporting Information of Figs. S10 and S11**).

A porous structure often enhances light absorbance because incident light can undergo multiple reflections and refractions within the material. As shown in Fig. 4**c**, the light absorbance of the dried MXene-based foam hydrogels was correlated with the MXene loading, such that higher MXene concentrations increased light absorption. As an example (P-F-
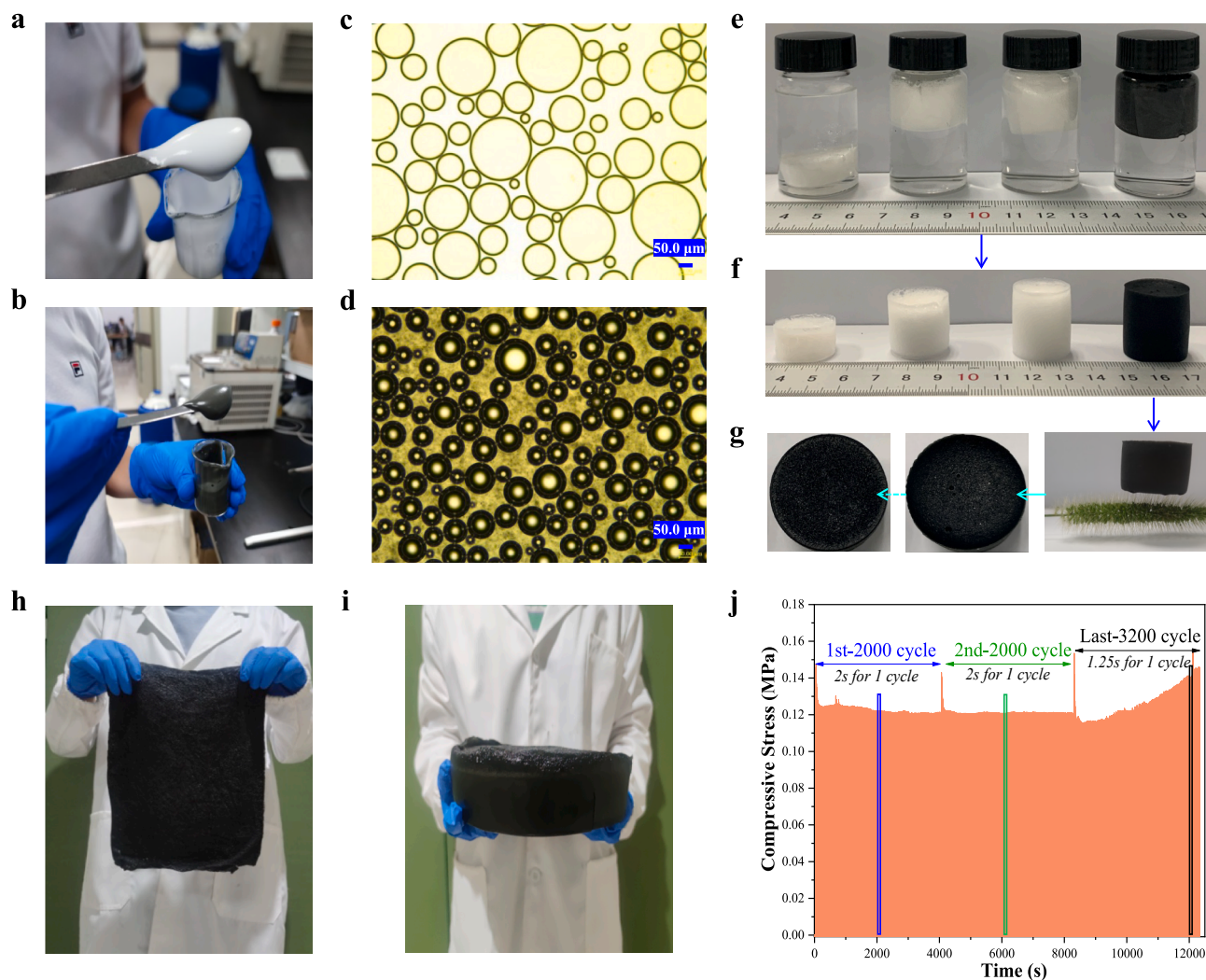
Fig. 2. (**a**) and (**b**) The bubble-filled PVA/F-127 and PVA/F-127/MXene systems, respectively. (**c**) and (**d**) Polarized optical microscopy images of the bubbles in (**a**) and (**b**), respectively. Images showing the floating behavior of PVA hydrogel, PVA foam hydrogel, PVA/F-127 and PVA/F-127/MXene foam hydrogels after cross-linking (from left to right) (**e**) and of wetted samples (**f**). (**g**) Photographs of a freeze-dried PVA/F-127/MXene foam hydrogel demonstrating the lightweight nature of the material and its rough top and bottom surfaces. (**h** and **i**) Large-scale preparation of PVA/F-127/MXene foam hydrogels. (**j**) The compressive fatigue resistance of the wet PVA/F-127/MXene foam hydrogel at an 80% compression ratio.

M−0.125), incorporating 0.125 mL of the MXene solution provided over 80% absorption in the UV region, approximate 80% in the visible region and over 75% in the infrared region. These values were also increased when the same sample was wetted with seawater and additional increases in the MXene content provided considerably higher solar absorption (Fig. 4d). The PVA/F-127/MXene specimen (P-F-M−1) made with 1 mL of the MXene solution provided over 96% absorption over the entire solar spectrum in the wet form. Fig. 4e summarizes the pore size distribution of the PVA-based foam hydrogels. Each of these specimens contained large pores with sizes primarily in the range of 10–100 μm, although some much larger pores (several hundred micrometers in size) were also identified. The incorporation of the F-127 and MXene promoted pore uniformity, reflected by decreases in the FWHM values of each plot. These results are in good agreement with the SEM images in Fig. 3. The porosity of these hydrogels is shown in Fig. 4f. Almost all the foam hydrogels had porosity values over 95%, representing the primary reason for the excellent compressibility and rapid water uptake shown by these materials.

The water transport behaviors and channel networks of the foam hydrogels containing MXenes were also examined by conducting numerical simulations. Fig. 4g provides the geometric model for the foam hydrogel material under the constraints of physical conditions while

Fig. 4h shows the meshing obtained after processing the model in Fig. 4g. In Fig. 4i, the overlapping circles in the COMSOL model represent interconnected pores containing liquid water or moist air. Water was pumped upward through the interconnected pores as a consequence of capillary forces and evaporated at the upper surface, which was exposed to 1 sun solar radiation. The large degree of pore interconnectivity provided pathways for the migration of liquid water and water vapor in nearly straight lines, indicating only minor diffusion-based resistance. The calculated total water and vapor transport velocities in each foam hydrogel were consistent with the experimental results (Fig. 4j). The static pressures induced by fluid motion in the hydrogel micro-channels without gravitational potential were calculated and are provided in Fig. 4k. A simple heat transfer model was also used to describe the temperature distribution in the P-F-M−0.25 sample (Fig. 4l). Simulations of the steady-state temperature distribution predicted that the maximum temperature at the surface of the polymeric surface of this material would be 41.85 °C. This predicted value was close to the experimental result (**Supporting Information of Fig. S12**), therefore confirming that heat nanoconfinement occurred in the foam hydrogels having various MXene concentrations.
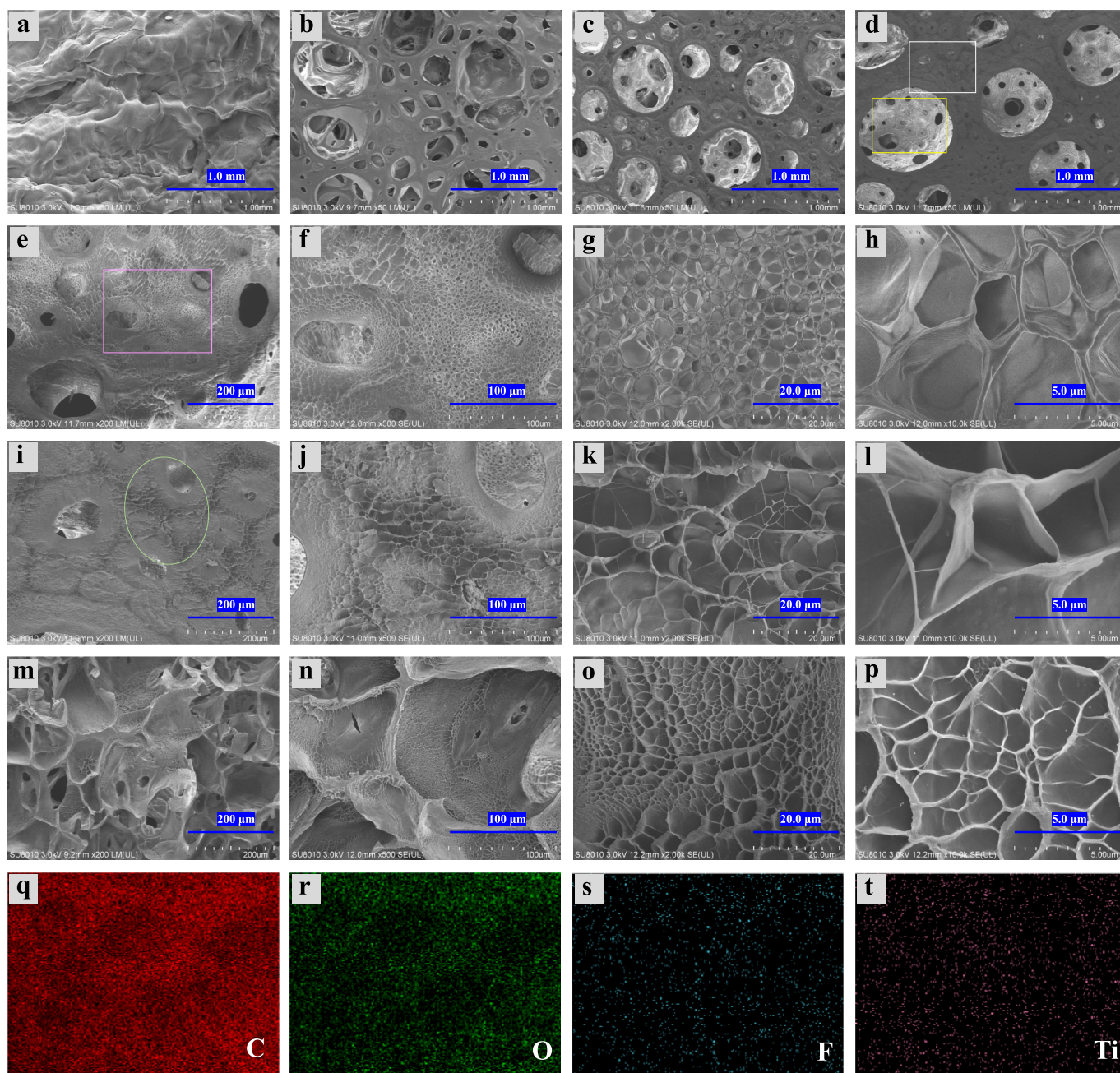
Fig. 3. SEM images showing the surface structures of the (**a**) PVA hydrogel, (**b**) PVA foam hydrogel, (**c**) PVA/F-127 foam hydrogel and (d) PVA/F-127/MXene foam hydrogel. (e-h) and (i-l) Magnified views of the regions outlined in yellow and white in (**d**) and additional magnifications of the regions outlined in pink and green in (**e**) and (**i**), respectively. (**m-p**) Images of the cross-sectional structure of the PVA/F-127/MXene foam hydrogel at various magnifications. (**q-t**) C, O, F and Ti elemental maps obtained from the PVA/F-127/MXene foam hydrogel.

3.4. Solar desalination performance

The present PVA/F-127/MXene foam hydrogels were studied as solar evaporators in two different forms, using either heat isolation (Fig. 5**a**) or heat supply models (Fig. 5**b**). As demonstrated in Fig. 5**a**, some of the solar evaporators were coated with a white thermally insulating foam (Fig. 5**a, left**) to block solar-induced photothermal energy along the horizontal direction from the central solar evaporator to the side walls of the container, which is currently the most popular strategy used. Upon exposure to solar radiation, these MXene-based solar evaporators presented a higher temperature, T_1, than that of the surrounding foam, T_2 (Fig. 5**a, right**). Theoretically, this model should provide limited water evaporation because heat losses will occur or there will be a temperature difference between the central part (having a high T_1) and its surroundings (having a low T_2). That is, based on simple thermodynamics, heat energy will be transferred from the high temperature region to the low temperature region. However, in the case that T_1 is lower than T_2, the central region could receive energy from its surroundings. This scenario occurs in the second mode as shown in Fig. 5**b**, in which a black foam replaces the white foam (Fig. 5**b, left**) and the foam hydrogel evaporator containing the MXene exhibits a considerably higher temperature. It should be noted that this elevated temperature is still lower relative to the surroundings of the black foam (Fig. 5**b**, right). That is, in this heat supply model, the PVA/F-127/MXene foam hydrogel loses little heat energy to its surroundings but can also obtain heat energy from its surroundings due to the black foam, which displays excellent photothermal properties.
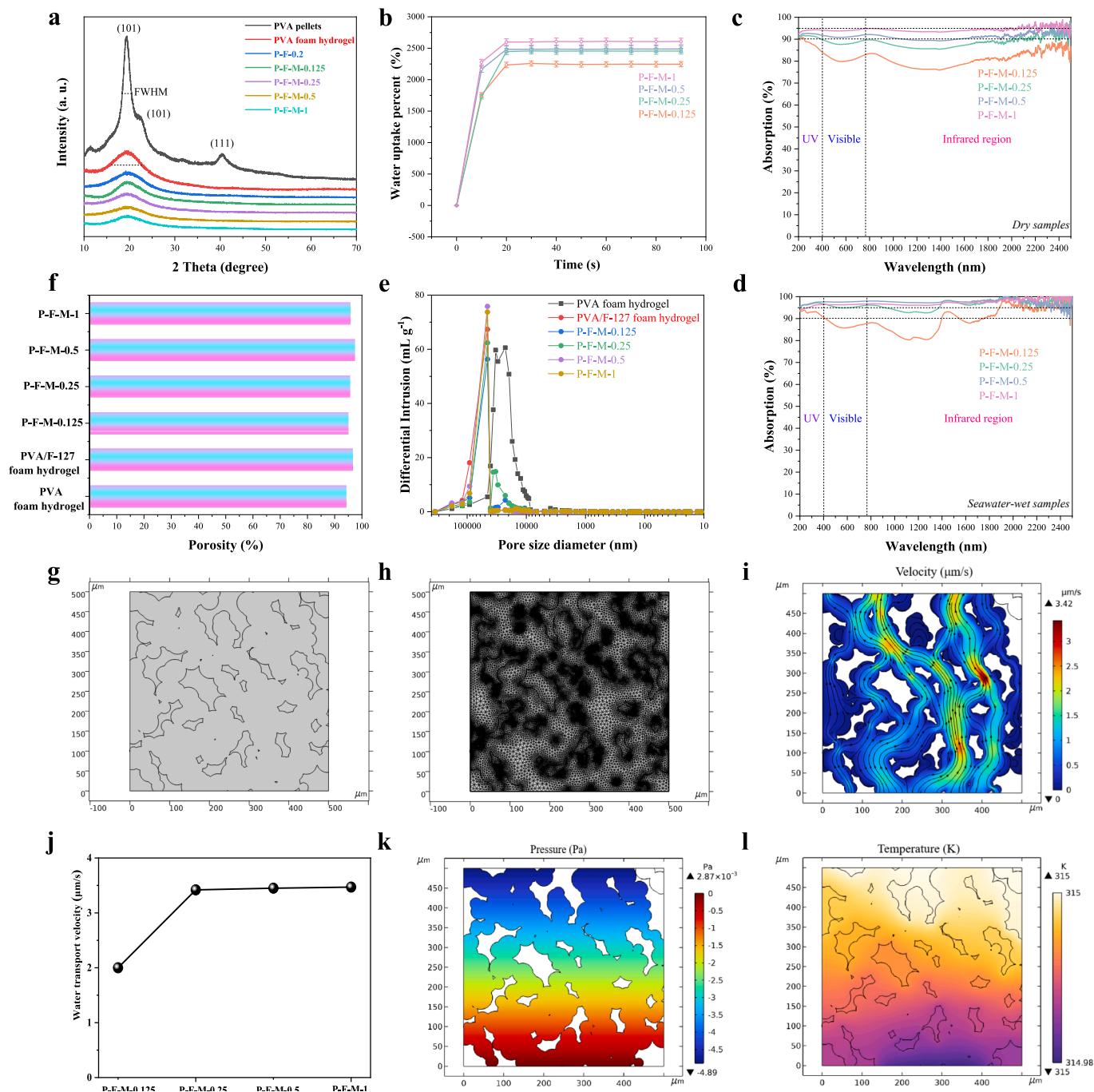
Fig. 4. Physical characterizations of PVA/F-127/MXene foam hydrogels and their counterparts. (**a**) XRD patterns. (**b**) Water uptake as a function of time. (**c**) and (**d**) Absorbance of the solar spectrum by dry and seawater-wet samples, respectively. (**e**) Pore size distributions and (**f**) calculated porosities of various specimens. Theoretical simulation results, including (**g**) the overall geometric modeling of the MXene-based integrated foam hydrogel and (**h**) meshing of hydrogels with various MXene contents generated using the COMSOL package. (**i**) Simulated water transport velocity mapping and low-tortuosity water pathways in the MXene-0.25 mL sample. (**j**) Water transport velocities in MXene-based integrated foam hydrogels as calculated using the COMSOL package. (**k**) Static pressures and (**l**) temperatures induced by the motion of water in micro-channels within the MXene-0.25 mL sample.

The utility of the heat supply model is demonstrated by the seawater evaporation data. Fig. 5c and 5d show the evaporation rates of seawater using the two evaporation models. These results indicate that the extent of water evaporation was greatly dependent on the MXenecontent, regardless of the evaporation model. This result was expected because samples having higher MXene contents showed improved light absorption and so better photothermal properties (meaning a higher T_1). More importantly, the evaporation model also greatly affected the performance of the system. As shown in Fig. 5e, when using the heat supply model, the sample with

the highest MXene loading showed an evaporation rate as high as 4.1 ± 0.1 kg m^{-2}h^{-1} with a corresponding energy efficiency of 128.8% ± 2.0% (Fig. 5f). Additionally, the evaporation rate still has a favorite evaporation cycle, as shown in Fig. 5g. This outstanding evaporation performance can be attributed to several factors. Firstly, the foam hydrogels showed lower ΔH_E values as a consequence of their unique porous structures that promoted the fraction of intermediate water [12]. As an example, the PVA-based foam hydrogels exhibited smaller ΔH_E values than that of bulk water (Fig. 5h). Furthermore, the introduction of the MXene further
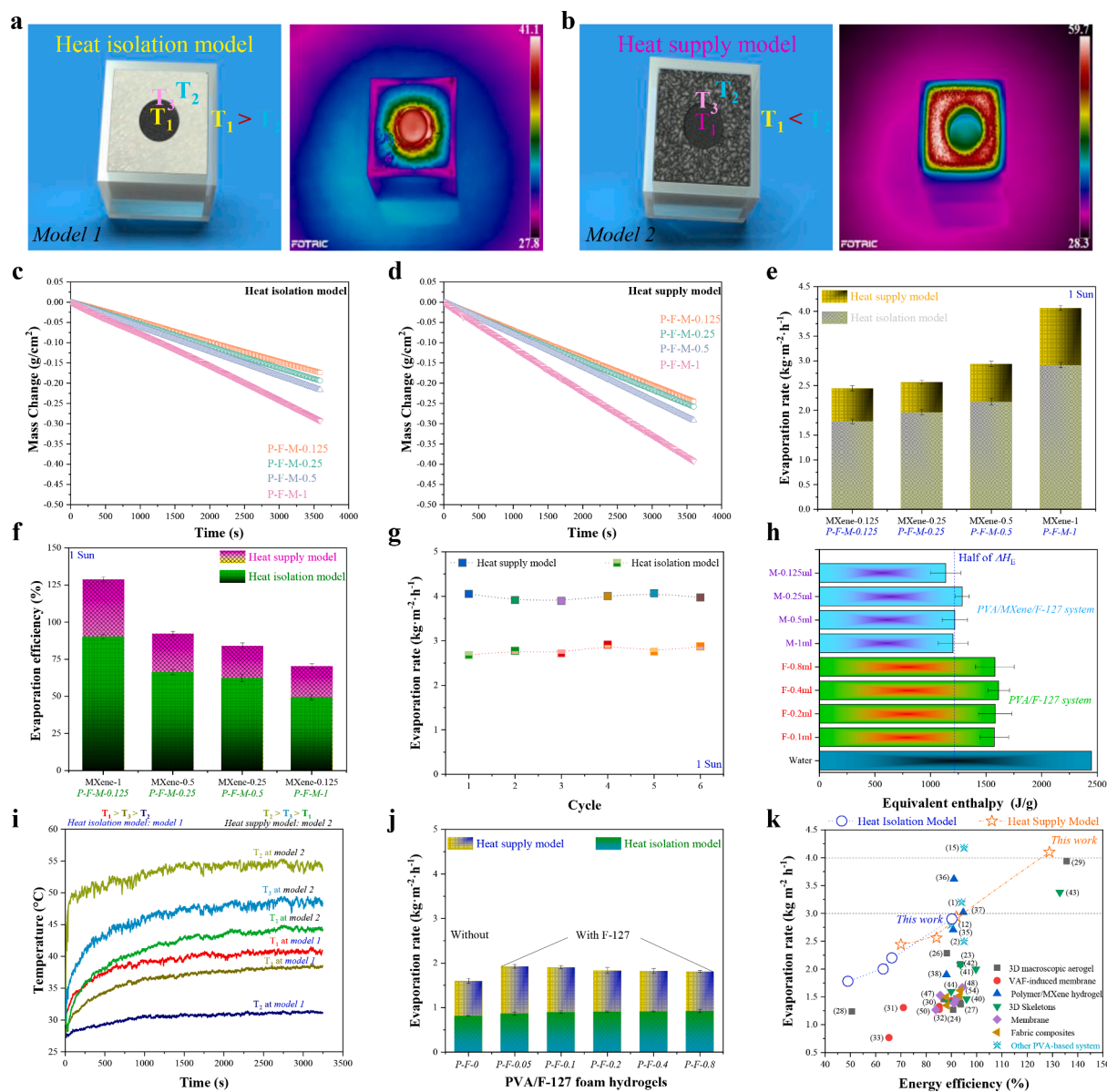
Fig. 5. The evaporation of actual seawater from PVA-based composites under 1 sun illumination. (**a**) *Model 1*: a heat isolation model [white foam + PVA/F-127/ MXene (P-F-M−1) foam hydrogel] and (**b**) *Model 2*: a heat supply model [black foam + PVA/F-127/MXene (P-F-M−1) foam hydrogel] used for evaporation trials and corresponding thermal images after a 10 min exposure to simulated sunlight. (**c**) and (**d**) Variations in seawater mass using PVA/F-127/MXene foam hydrogels with various MXene contents as the evaporators together with the thermal insulation model and heat supply model, respectively. (**e**) and (**f**) corresponding evaporation rates and energy efficiencies, respectively. (**g**) Cycling stability of the evaporation performance of the PVA/F-127/MXene (P-F-M−1) foam hydrogel with the two evaporation models. (**h**) ΔH_E values of bulk water and water within the PVA-based foam hydrogels. (**i**) Temperature changes as functions of irradiation time for the PVA/F-127/MXene foam hydrogel using the two evaporation models. (**j**) Evaporation rates of PVA/F-127 systems with the two evaporation models. (**k**) Comparison of evaporation rate and energy efficiency under 1 sun irradiation with the previous literature.

lowered ΔH_E (Fig. 5h). It is speculated that both F-127 and MXene nanosheets elevated surface viscosity of the foam film and that hindered flow and discharge of liquid on the foam film, leading to effective depression of foam film drainage and also reduction of bubbles' size of the PVA based foams. Secondly, the heat supply evaporation model allowed the sample heater to indirectly obtain additional energy from solar radiation through the black foam even in PVA/F-127 cases, thus increasing the rate of evaporation as well as the energy efficiency (over 100%). The clear comparison of photoinduced temperatures (T₁, T₂ and T₃) in Fig. 5i within the both evaporation models again confirms such a speculation. In fact, thanks to these advantages, PVA/F-127 foam hydrogels without MXene also present enhanced evaporation performances in Fig. 5j. It needs to be emphasized that both white and black foams used in this study could not provide helpful evaporation areas to participate in the whole evaporation

process due to their extremely low evaporation rate of seawater under the same conditions (**Supporting Information of Fig. S13**). Lastly, the rapid water transport in these materials continuously supplied fresh water for evaporation and avoided the precipitation of salt crystals that can occur with a slower water supply. Despite effects of MXene-based nanocomposites in years to construct evaporation systems, evaporation performance improvement is still challenging. The PVA/MXene/F-127 (P-F-M−1) foam hydrogel clearly outperforms almost all of the reported MXene-based synthetic materials and ranks at the top of the comparison chart in Fig. 5k (**Supporting information of Table S2**).

The seawater evaporation performance of a system based on the PVA/F-127/MXene (P-F-M−1) foam hydrogel under natural sunlight in an outdoor setting is summarized in Fig. 6. A typical evaporation system, including a transparent optical quartz condenser and a peristaltic pump

providing a continuous seawater supply, is shown in Fig. 6a, while Fig. 6b shows a heat supply model. The concentrations of various ions in the collected fresh water are summarized in Fig. 6c. It is evident that the evaporated water contained significantly reduced ion concentrations that met the World Health Organization (1‰) requirements [1,2,15]. The evaporation of a sample was monitored between 8:00 a.m. and 6:00p.m. over a 32-day period. As an example, Fig. 6d presents the data obtained on Sep. 17, 2022, at Shenzhen University's Canghai campus. The highest evaporation rate of 3.1 kg m^{-2}h^{-1} was observed at approximately noon. Interestingly, this value was lower than that of 4.1 kg m^{-2}h^{-1} obtained from experiments in the laboratory. This discrepancy is attributed to the relatively low intensity of the natural sunlight (only 0.85 sun). Additionally, although the large-scale sample and black foam used in the outdoor tests were prepared at the same volume ratio used in the laboratory experiments, the larger MXene/PVA foam hydrogel in the center of this device may not have absorbed sufficient heat from the black foam because of its greatly increased surface area relative to the smaller quantity used in the laboratory trials. A long-term stability test was performed from Sep. 4 to Oct. 6, 2022, during which the sample was replaced at 10 day intervals. The data indicate that, throughout a 32 day period, a high evaporation rate between 2.5 and 3.0 kg m^{-2}h^{-1} was obtained between 11:00 a.m. and 3:00p.m. on 41% of the days (Fig. 6e), whereas 13% of the days during this time period showed an evaporation rate in excess of 3.0 kg m^{-2}h^{-1}. This performance is considered reasonable because only 18% of the days in this period had a sunlight intensity between 0.8 and 0.9 sun and just 25% had an intensity between

0.9 and 1 sun (Fig. 6f). That is, the present system exhibited high evaporation rates under relatively weak sunlight. The resistance values of various purified water specimens were determined (Fig. 6g) and the purified water obtained from this apparatus showed a comparable resistance (4.07 MΩ) with that of deionized laboratory water (4.71 MΩ) and drinking water (4.36 MΩ) obtained from the Dasha River Park in Shenzhen, China, indicating a high purity. However, the resistance of the evaporated water was clearly lower than that of domestic drinking water (5.29 MΩ) that had been passed through a commercial filter. Thus, the collected water had a lower ion content than the laboratory running water (1.648 MΩ) and a much lower ion concentration compared with the original seawater (253.6 kΩ).

4. Conclusions

PVA/MXene-based foam hydrogels were prepared via a simple strategy involving high-speed stirring and cross-linking. Employing a foam phase inversion concept, we realized hierarchical pore-in-pore structures in these materials. The as-prepared foam hydrogels greatly decreased the enthalpy of water evaporation, while providing rapid water transport and uptake (with a value of 175%/s). The foam hydrogels were robust and could be compressed at least 7000 times at 80% strain, while exhibiting excellent solar absorption (over 96% over the entire solar spectrum). Using a newly developed heat supply model, an outstanding evaporation rate of 4.1 ± 0.1 kg m^{-2}h^{-1} and an energy efficiency of 128.8% ± 2.0% were obtained. These systems
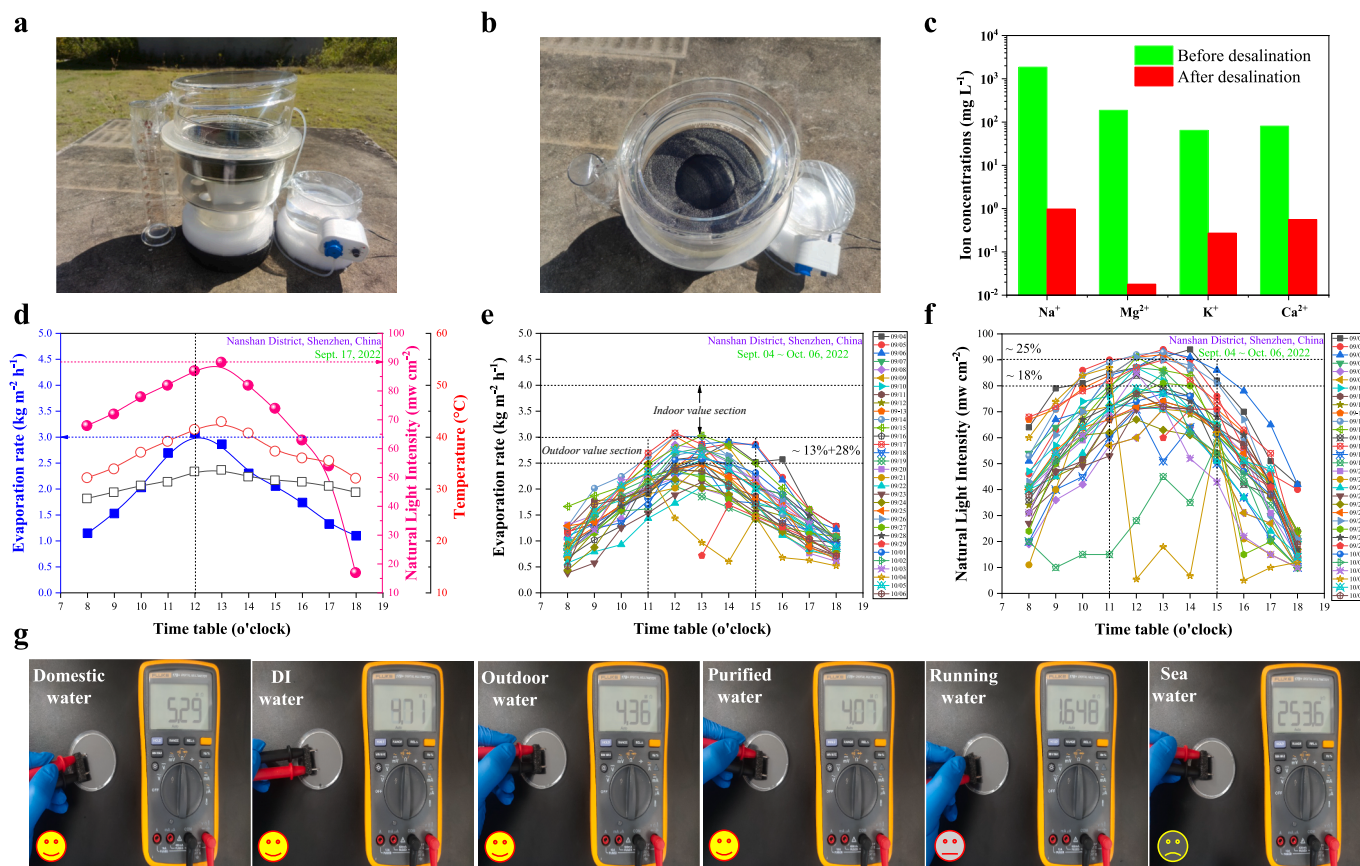

Fig. 6. An outdoor solar seawater purification system using the PVA/F-127/MXene foam hydrogel as an evaporator material under natural sunlight. (**a**) Photographic image of the purification system including the transparent optical quartz condenser and peristaltic pump used to provide a continuous seawater supply. (**b**) Photographic image of a large-scale PVA/F-127/MXene foam hydrogel specimen encased in a commercially available black foam to construct a heat supply evaporation model. (**c**) Ion concentrations of seawater before and after desalination. (**d**) Evaporation rates and light intensity data obtained over an 11 h outdoor solar desalination trial on Sep. 17, 2022, at Shenzhen University, Shenzhen, China. (**e**) and (**f**) Real time evaporation rates and light intensity data obtained during a trial running from Sep. 4, 2022 to Oct. 6, 2022 at Shenzhen University, Shenzhen, China. (**g**) Evaluation of water purity by comparing their resistance values with common types of drinking water and water from the laboratory.

outperformed almost all MXene-based evaporation systems and other traditional systems reported to date. Thus, our foam hydrogels have great potential to be employed in long-term, high-efficiency solar interfacial evaporation applications.

Declaration of Competing Interest

The authors declare that they have no known competing financial interests or personal relationships that could have appeared to influence the work reported in this paper.

Data availability

Data will be made available on request.

Appendix A. Supplementary data

Supplementary data to this article can be found online at https://doi.org/10.1016/j.cej.2023.142409.

References

[1] F. Zhao, X. Zhou, Y.e. Shi, X. Qian, M. Alexander, X. Zhao, S. Mendez, R. Yang, L. Qu, G. Yu, Highly efficient solar vapour generation via hierarchically nanostructured gels, Nat. Nanotech. 13 (6) (2018) 489–495.

[2] X. Zhou, F. Zhao, Y. Guo, Y. Zhang, G. Yu, A Hydrogel-Based Antifouling Solar Evaporator for Highly Efficient Water Desalination, Energy Environ. Sci. 11 (2018) 1985–1992, https://doi.org/10.1039/c8ee00567b.

[3] Y. Guo, X. Zhou, F. Zhao, J. Bae, B. Rosenberger, G. Yu, Synergistic Energy Nanoconfinement and Water Activation in Hydrogels for Efficient Solar Water Desalination, ACS Nano 13 (2019) 7913–7919.

[4] F. Zhao, Y. Guo, X. Zhou, W. Shi, G. Yu, Materials for solar-powered water evaporation, Nat. Rev. Mater. 5 (2020) 388–401.

[5] X. Zhou, Y. Guo, G.Y. Zhao, Hydrogels as an Emerging Material Platform for Solar Water Purification, Acc. Chem. Res. 52 (2019) 3244–3253.

[6] Y. Guo, G. Yu, Engineering Hydrogels for Efficient Solar Desalination and Water Purification, Acc. Mater. Res. 2 (2021) 374–384.

[7] Y. Guo, J. Bae, Z. Fang, P. Li, F. Zhao, G. Yu, Hydrogels and Hydrogel-Derived Materials for Energy and Water Sustainability, Chem. Rev. 120 (2020) 7642–7707.

[8] X. Zhou, F. Zhao, P. Zhang, G. Yu, Solar Water Evaporation Toward Water Purification and Beyond, ACS Materials Lett. 3 (2021) 1112–1129.

[9] X. Zhou, F. Zhao, Y. Guo, B. Rosenberger, G. Yu, Architecting Highly Hydratable Polymer Networks to Tune the Water State for Solar Water Purification, Sci. Adv. 5 (2019) eaaw5484.

[10] Y. Guo, F. Zhao, X. Zhou, Z. Chen, G. Yu, Tailoring Nanoscale Surface Topography of Hydrogel for Efficient Solar Vapor Generation, Nano Lett. 19 (2019) 2530–2536.

[11] Y. Guo, X. Zhao, F. Zhao, Z. Jiao, X. Zhou, G. Yu, Tailoring Surface Wetting States for Ultrafast Solar-Driven Water Evaporation, Energy Environ. Sci. 13 (2020) 2087–2095.

[12] Y. Guo, L.S. Vasconcelos, N. Manohar, J. Geng, K.P. Johnston, G. Yu, Highly Elastic Interconnected Porous Hydrogels through Self-Assembled Templating for Solar Water Purification, Angew. Chem. Int. Ed. 61 (3) (2022) e202114074.

[13] H. Yang, Z. Li, B. Lu, J. Gao, X. Jin, G. Sun, G. Zhang, P. Zhang, L. Qu, Reconstruction of Inherent Graphene Oxide Liquid Crystals for Large-Scale Fabrication of Structure-Intact Graphene Aerogel Bulk toward Practical Applications, ACS Nano 12 (2018) 11407–11416.

[14] X. Zhang, T. Zhang, Z. Wang, Z. Ren, S. Yan, Y. Duan, J. Zhang, Ultralight, Superelastic, and Fatigue-Resistant Graphene Aerogel Templated by Graphene Oxide Liquid Crystal Stabilized Air Bubbles, ACS Appl. Mater. Interfaces 11 (2019) 1303–1310.

[15] C. Ma, Q. Liu, Q. Peng, G. Yang, M. Jiang, L. Zong, J. Zhang, Biomimetic Hybridization of Janus-like Graphene Oxide into Hierarchical Porous Hydrogels for Improved Mechanical Properties and Efficient Solar Desalination Devices, ACS Nano 15 (2021) 19877–19887.

[16] M. Naguib, M. Kurtoglu, V. Presser, J. Lu, J. Niu, M. Heon, L. Hultman, Y. Gogotsi, M.W. Barsoum, Two-Dimensional Nanocrystals Produced by Exfoliation of Ti$_3$AlC$_2$, Adv. Mater. 23 (37) (2011) 4248–4253.

[17] K. Huang, Z. Li, J. Lin, G. Han, P. Huang, Two-dimensional transition metal carbides and nitrides (MXenes) for biomedical applications, Chem. Soc. Rev. 47 (2018) 5109–5124.

[18] Y. Zhang, J.K. El-Demellawi, Q. Jiang, G. Ge, K. Laing, X. Lee, H.A. Dong, MXene Hydrogels: Fundamentals and Applications, Chem. Soc. Rev. 49 (2020) 7229–7251.

[19] M. Hu, H. Zhang, T. Hu, B. Fan, X. Wang, Z. Li, Emerging 2D MXenes for Supercapacitors: Status, Challenges and Prospects, Chem. Soc. Rev. 49 (18) (2020) 6666–6693.

[20] R. Li, L. Zhang, P. Wang, MXene Ti$_3$C$_2$: An Effective 2D Light-to-Heat Conversion Material, ACS Nano 11 (2017) 3752–3759.

[21] F. Shahzad, M. Alhabeb, C. Hatter, B. Anasori, S.M. Hong, C.M. Koo, Y. Gogotsi, Electromagnetic Interference Shielding with 2D Transition Metal Carbides (MXenes), Science 353 (2016) 1137–1140.

[22] Q. Zhang, G. Yi, Z. Fu, H. Yu, S. Chen, X. Quan, Vertically Aligned Janus MXene-Based Aerogels for Solar Desalination with High Efficiency and Salt Resistance, ACS Nano 13 (2019) 13196–13207.

[23] W. Li, X. Li, W. Chang, J. Wu, P. Liu, J. Wang, X.i. Yao, Z.-Z. Yu, Vertically Aligned Reduced Graphene Oxide/Ti$_3$C$_2$T$_x$ MXene Hybrid Hydrogel for Highly Efficient Solar Steam Generation, Nano Res. 13 (11) (2020) 3048–3056.

[24] X. Ming, A. Guo, Q. Zhang, Z. Guo, F. Yu, B. Hou, Y. Wang, K.P. Homewood, X. Wang, 3D Macroscopic Graphene Oxide/MXene Architectures for Multifunctional Water Purification, Carbon 167 (2020) 285–295.

[25] X. Fan, Y. Yang, X. Shi, Y. Liu, H. Li, J. Liang, Y. Chen, A MXene-Based Hierarchical Design Enabling Highly Efficient and Stable Solar-Water Desalination with Good Salt Resistance, Adv. Funct. Mater. 30 (52) (2020) 2007110.

[26] X. Han, S. Ding, L. Fan, Y. Zhou, S. Wang, Janus Biocomposite Aerogels Constituted of Cellulose Nanofibrils and MXenes for Application as Single-Module Solar-Driven Interfacial Evaporators, J. Mater. Chem. A 9 (34) (2021) 18614–18622.

[27] Z. Ai, Y. Zhao, R. Gao, L. Chen, T. Wen, W. Wang, T. Zhang, W. Ge, S. Song, Self-Assembly Hierarchical Binary Gel Based on MXene and Montmorillonite Nanosheets for Efficient and Stable Solar Steam Generation, J. Clean. Prod 357 (2022), 132000.

[28] Z. Zheng, H. Liu, D. Wu, X. Wang, Polyimide/MXene Hybrid Aerogel-Based Phase-Change Composites for Solar-Driven Seawater Desalination, Chem. Eng. J. 440 (2022), 135862.

[29] X. Li, X. Li, H. Li, Y. Zhao, J. Wu, S. Yan, Z. Yu, Reshapable MXene/Graphene Oxide/Polyaniline Plastic Hybrids with Patternable Surfaces for Highly Efficient Solar-Driven Water Purification, Adv. Funct. Mater. 32 (2022) 2110636.

[30] P. Ying, B. Ai, W. Hu, Y. Geng, L. Li, K. Sun, S.C. Tan, W. Zhang, M. Li, A Bio-Inspired Nanocomposite Membrane with Improved Light-Trapping and Salt-Rejecting Performance for Solar-Driven Interfacial Evaporation Applications, Nano Energy 89 (2021), 106443, https://doi.org/10.1016/j.nanoen.2021.106443.

[31] J. Zhao, Y. Yang, C. Yang, Y. Tian, Y. Han, J. Liu, X. Yin, W. Que, A Hydrophobic Surface Enabled Salt-Blocking 2D Ti$_3$C$_2$ MXene Membrane for Efficient and Stable Solar Desalination, J. Mater. Chem. A 6 (33) (2018) 16196–16204.

[32] X. Zhao, X.-J. Zha, L.-S. Tang, J.-H. Pu, K. Ke, R.-Y. Bao, Z.-Y. Liu, M.-B. Yang, W. Yang, Self-Assembled Core-Shell Polydopamine@MXene with Synergistic Solar Absorption Capability for Highly Efficient Solar-to-Vapor Generation, Nano Res. 13 (1) (2020) 255–264.

[33] M. Mustakeem, J.K. El-Demellawi, M. Obaid, F. Ming, H.N. Alshareef, N. Ghaffour, MXene-Coated Membranes for Autonomous Solar-Driven Desalination, ACS Appl. Mater. Interfaces 14 (2022) 5265–5274.

[34] Y. Wang, J. Nie, Z. He, Y. Zhi, X. Ma, P. Zhong, Ti$_3$C$_2$T$_x$ MXene Nanoflakes Embedded with Copper Indium Selenide Nanoparticles for Desalination and Water Purification through High Efficiency Solar-Driven Membrane Evaporation, ACS Appl. Mater. Interfaces 14 (2022) 5876–5886.

[35] Z. Yu, P. Wu, Biomimetic MXene-Polyvinyl Alcohol Composite Hydrogel with Vertically Aligned Channels for Highly Efficient Solar Steam Generation, Adv. Mater. Technol. 5 (2020) 2000065.

[36] Y. Lu, D. Fan, Y. Wang, H. Xu, C. Lu, X. Yang, Surface Patterning of Two-Dimensional Nanostructure-Embedded Photothermal Hydrogels for High-Yield Solar Steam Generation, ACS Nano 15 (2021) 10366–10376.

[37] M. Pi, X. Wang, Z. Wang, R. Ran, Sustainable MXene/PDA Hydrogel with Core-Shell Structure Tailored for Highly Efficient Solar Evaporation and Long-term Desalination, Polymer 230 (2021), 124075.

[38] H. Zhang, X. Shen, E. Kim, M. Wang, J. Lee, H. Chen, G. Zhang, J.K. Kim, Integrated Water and Thermal Managements in Bioinspired Hierarchical MXene Aerogels for Highly Efficient Solar-Powered Water Evaporation, Adv. Funct. Mater. 32 (2022) 2111794.

[39] X. Zhao, X.-J. Zha, J.-H. Pu, L.u. Bai, R.-Y. Bao, Z.-Y. Liu, M.-B. Yang, W. Yang, Macroporous Three-Dimensional MXene Architectures for Highly Efficient Solar Steam Generation, J. Mater. Chem. A 7 (17) (2019) 10446–10455.

[40] N. Ma, Q. Fu, Y. Hong, X. Hao, X. Wang, J. Ju, J. Sun, Processing Natural Wood into an Efficient and Durable Solar Steam Generation Device, ACS Appl. Mater. Interfaces 12 (2020) 18165–18173.

[41] Y.i. Yang, W. Fan, S. Yuan, J. Tian, G. Chao, T. Liu, A 3D-Printed Integrated MXene-Based Evaporator with a Vertical Array Structure for Salt-Resistant Solar Desalination, J. Mater. Chem. A 9 (42) (2021) 23968–23976.

[42] Y. Chen., J. Yang, L. Zhu, X. Jia, S. Wang, Y. Li, H. Song, H. An Integrated Highly Hydrated Cellulose Network with a Synergistic Photothermal Effect for Efficient Solar-Driven Water Evaporation and Salt Resistance, J. Mater. Chem A 9 (2021) 15482–15492.

[43] W. Li, X. Tian, X. Li, J. Liu, C. Li, X. Feng, C. Shu, Z. Yu, An Environmental Energy-Enhanced Solar Steam Evaporator Derived from MXene-Decorated Cellulose Acetate Cigarette Filter with Ultrahigh Solar Steam Generation Efficiency, J. Colloid Interf. Sci. 606 (2022) 748–757.

[44] Y. Jin, K. Wang, S. Li, J. Liu, Encapsulation of MXene/Polydopamine in Nitrogen-Doped 3D Carbon Networks with High Photothermal Conversion Efficiency for Seawater Desalination, J. Colloid Interf. Sci. 614 (2022) 345–354.

[45] H. Guan, T. Fan, H. Bai, Y. Su, Z. Liu, X. Ning, M. Yu, S. Ramakrishna, Y. Long, A Waste Biomass-Derived Photothermic Material with High Salt resistance for Efficient Solar Evaporation, Carbon 188 (2021) 265–275.

[46] J. Fei, S.W. Koh, W. Tu, J. Ge, h. Rezaeyan, S. Hou, H. Duan, Y.C. Lam, H. Li, Functionalized MXene Enabled Sustainable Water Harvesting and Desalination, Adv. Sustain. Syst. 4 (2020) 2000102.

[47] H. Li, L. Li, L. Xiong, G. Wang, S. Ma S, X. Han, SiO$_2$/MXene/Poly (tetrafluoroethylene)-Based Janus Membranes as Solar Absorbers for Solar Steam Generation, ACS Appl. Nano Mater. 4 (2021) 14274−14284.

[48] X.P. Li, X. Li, H. Li, Y. Zhao, W. Li, S. Yan, Z.Z. Yu, 2D Ferrous Ion-Crosslinked Ti$_3$C$_2$T$_x$ MXene Aerogel Evaporators for Efficient Solar Steam Generation, Adv. Sustainable Syst. 5 (12) (2021) 2100263, https://doi.org/10.1002/adsu.202100263.

[49] C. Cai, Y. Wang, Z. Wei, Y. Fu, Biomimetic 3D Membranes with MXene Heterostructures for Superior Solar Steam Generation, Water Treatment, and Electricity Generation, Sol. RRL 5 (2021) 2100593.

[50] Z. Wang, W. Xu, K. Yu, S. Gong, H. Mao, R. Huang, Z. Zhu, NiS$_2$ Nanocubes Coated Ti$_3$C$_2$ Nanosheets with Enhanced Light-to-Heat Conversion for Fast and Efficient Solar Seawater Steam Generation, Sol. RRL 5 (2021) 2100183.

[51] Y. Wang, Q. Qi, J. Fan, W. Wang, D. Yu, Simple and Robust MXene/Carbon Nanotubes/Cotton Fabrics for Textile Wastewater Purification via Solar-Driven Interfacial Water Evaporation, Sep. Purif. Technol. 254 (2021), 117615.

[52] X. Xiao, J. Yan, S. Gao, X. Huang, J. Luo, L. Wang, S. Zhang, Z. Wu, X. Lai, J. Gao, Superhydrophobic MXene Based Fabric Composite for High Efficiency Solar Desalination, Desalination 524 (2022), 115475.

[53] Z. Wu, J. Li, S. Zhang, J. Yan, J. Gao, N. Zheng, H. Xu, Chitosan Assisted MXene Decoration onto Polymer Fabric for High Efficiency Solar Driven Interfacial Evaporation of Oil Contaminated Seawater, J. Colloid Interf. Sci. 622 (2022) 169–180.

[54] Z. Lei, X. Sun, S. Zhu, K. Dong, X. Liu, L. Wang, X. Zhang, L. Qu, X. Zhang, Nature Inspired MXene-Decorated 3D Honeycomb-Fabric Architectures Toward Efficient Water Desalination and Salt Harvesting, Nano-Micro Lett. 14 (1) (2022) 10.

[55] C. Xing, Y. Tian, Z. Yu, Z. Li, B. Meng, Z. Peng, Cellulose Nanofiber-Reinforced MXene Membranes as Stable Friction Layers and Effective Electrodes for High-Performance Triboelectric Nanogenerators, ACS Appl. Mater. Interfaces 14 (2022) 36741–36752.